Full-bandwidth electrophysiology of seizures and epileptiform activity enabled by flexible graphene microtransistor depth neural probes

Andrea Bonaccini Calia[1], Eduard Masvidal-Codina[2,3], Trevor M. Smith[4], Nathan Schäfer[1],
Daman Rathore[4], Elisa Rodríguez-Lucas[1], Xavi Illa[2,3], Jose M. De la Cruz[1], Elena Del Corro[1],
Elisabet Prats-Alfonso[2,3], Damià Viana[1], Jessica Bousquet[1], Clement Hébert[1], Javier Martínez-Aguilar[2,3],
Justin R. Sperling[1], Matthew Drummond[5], Arnab Halder[5], Abbie Dodd[5], Katharine Barr[5],
Sinead Savage[5], Jordina Fornell[6], Jordi Sort[6,7], Christoph Guger[8], Rosa Villa[2,3],
Kostas Kostarelos[1,5], Rob C. Wykes[4,5 ✉], Anton Guimerà-Brunet[2,3 ✉] and Jose A. Garrido[1,7 ✉]

Mapping the entire frequency bandwidth of brain electrophysiological signals is of paramount importance for understanding physiological and pathological states. The ability to record simultaneously DC-shifts, infraslow oscillations (<0.1 Hz), typical local field potentials (0.1–80 Hz) and higher frequencies (80–600 Hz) using the same recording site would particularly benefit preclinical epilepsy research and could provide clinical biomarkers for improved seizure onset zone delineation. However, commonly used metal microelectrode technology suffers from instabilities that hamper the high fidelity of DC-coupled recordings, which are needed to access signals of very low frequency. In this study we used flexible graphene depth neural probes (gDNPs), consisting of a linear array of graphene microtransistors, to concurrently record DC-shifts and high-frequency neuronal activity in awake rodents. We show here that gDNPs can reliably record and map with high spatial resolution seizures, pre-ictal DC-shifts and seizure-associated spreading depolarizations together with higher frequencies through the cortical laminae to the hippocampus in a mouse model of chemically induced seizures. Moreover, we demonstrate the functionality of chronically implanted devices over 10 weeks by recording with high fidelity spontaneous spike-wave discharges and associated infraslow oscillations in a rat model of absence epilepsy. Altogether, our work highlights the suitability of this technology for in vivo electrophysiology research, and in particular epilepsy research, by allowing stable and chronic DC-coupled recordings.

Pathological electrophysiological signals resulting from epilepsy span a wide frequency range, from fast activity, at hundreds of hertz or higher, to less explored signals below 0.1 Hz, including DC-shifts (sustained over seconds to minutes) and infraslow oscillations[1–3]. In contrast to the widely used AC-coupled recordings, DC-coupled recordings allow more comprehensive assessment of the pathophysiological processes associated with either an increase in neuronal activity during seizures or a loss of neuronal activity during a spreading depolarization (SD)[4]. Clinically, electrophysiological biomarkers have been explored to guide surgical resection of the seizure onset zone[5,6]; however, improvement and refinements are still needed[7,8]. Indeed, intracranial clinical studies using large metallic electrodes suggest that the efficacy of current electrophysiological biomarkers could be improved by the inclusion of DC-shifts[9]. However, broad adoption of DC-shifts as a novel biomarker is limited by the poor capabilities of microelectrode technology to reliably record this type of electrophysiological signal in vivo with high spatiotemporal fidelity. This is due to

polarization-induced drift and signal attenuation causing distortion of the measured signal by metallic electrodes[10–12]. Currently, the gold standard for high-fidelity DC-coupled recordings is the glass micropipette; however, its use is limited to few-point measurements, hampering the spatial resolution required for seizure localization, and is not suitable for clinical applications. An alternative to commonly used passive electrodes are field-effect transistors (FETs), which are active transducers offering important advantages in electrophysiology[13]. Among the few FET technologies that have been validated for in vivo electrophysiology, graphene-based FETs are particularly attractive because of the combination of material properties, including chemical and electrochemical inertness, high electrical mobility, biocompatibility, as well as facile integration into flexible and ultrathin substrates[14]. Recent reports demonstrate the potential of graphene solution-gated field-effect transistors (gSGFETs) for neural interfacing[15,16]. A proof-of-concept of high-fidelity DC-coupled recordings enabled by gSGFETs was demonstrated by mapping chemically induced cortical SDs in anaesthetized rats[17]. To explore

its usefulness for epilepsy research, we have developed implantable, flexible graphene depth neural probes (gDNPs) capable of recording localized full-bandwidth neuronal activity through cortical columns and subcortical structures. Here, we present a wafer-scale microtechnology process to fabricate ultrathin gDNPs consisting of a linear array of graphene microtransistors imbedded in a polymeric flexible substrate. To penetrate through the mouse cortex and reach the hippocampus without buckling, we adapted an insertion protocol that uses silk fibroin (SF)[18,19] to temporarily stiffen flexible gDNPs. The ability to detect electrophysiological biomarkers of epileptiform activity in preclinical rodent models of induced seizures and chronic epilepsy has been validated experimentally[20]. These included seizure events such as spike-and-wave discharges (SWDs)[21] and high-frequency oscillations (HFOs)[22,23]. Additionally, we highlight the suitability of graphene transistor technology to record concurrently fast and slow brain electrophysiological signals by benchmarking against a solution-filled glass micropipette recording, demonstrating the high fidelity of the DC-coupled recordings obtained by the gDNPs. Here, we demonstrate the capability of gDNPs to record both active and passive ictal baseline shifts[24-26] as well as SD associated with seizure activity. Altogether, our results illustrate the potential of graphene microtransistor technology to reveal mechanistic insights into the involvement of infra-slow oscillations and DC-shifts associated with seizures in vivo in awake brain.

Microfabrication, characterization and stiffening of the gDNPs

A graphene-based SGFET is a three-terminal device in which single-layer graphene prepared by chemical vapour deposition (CVD) is used as the channel material in contact with the drain and source terminals. Graphene is the sensing part of the device directly exposed to the neural tissue. The current in the graphene channel can be modulated or pinned by a third terminal given by a reference electrode (gate), which is also in contact with the conducting neural tissue (Fig. 1a). Thus, variations in the electrical potential in the tissue can be transduced into variations in the channel current; this transduction mechanism has been shown to offer a very versatile sensing platform for electrophysiology[27,28]. The flexible gDNP prepared in this study consists of a linear array of 14 recording transistors, each with an active area of $60 \times 60\,\mu m^2$, and a pitch of $100\,\mu m$. The probe's tip design consists of a polyimide shank of $200\,\mu m$ width and $1.6\,mm$ length (Fig. 1b). A gDNP design with smaller SGFETs ($20 \times 20\,\mu m^2$) and narrower shank ($150\,\mu m$ width) has also been fabricated (Supplementary Fig. 1). The gDNPs were fabricated on a 10-μm-thick flexible polyimide (PI) substrate using a wafer-scale microfabrication process previously reported[16] (Methods). A two-level metallization strategy, with the metal levels interconnected by via holes (Fig. 1b), reduces track resistance and improves sensor performance. To characterize gDNPs in saline solution we simultaneously measure the drain–source current (I_{DS}) versus the applied gate–source voltage (V_{GS}) for all the transistors on the shank with a fixed drain–source voltage (V_{DS}) using customized electronics (Methods). gSGFETs exhibit very high transconductance (g_m) values due to direct contact with the tissue, possible as a result of its biocompatibility and electrochemical inertness, and to the very high charge carrier mobility of graphene[29]. Figure 1c shows the transfer curves as well as the normalized transconductance ($|g_m| = g_m/V_{DS}$) for all 14 gSGFETs of an exemplary gDNP device. The small dispersion of the charge neutrality point (CNP), defined as the value of V_{GS} where the I_{DS} reaches a minimum, attests to the homogeneity of the gDNP. Furthermore, g_m shows a very stable response over a wide applied gate frequency range (up to 5 kHz), both in the hole regime, $V_{GS} < V_{CNP}$, and in the electron regime, $V_{GS} > V_{CNP}$ (Fig. 1d). Such a constant frequency response is important for a proper calibration of the recorded signals[30]. The detection

limit of the sensors was evaluated by means of the effective gate noise (that is, root-mean-square gate voltage noise, V_{RMS}) integrated between 1 Hz and 2 kHz, with averaged values of 25–30 μV for all fabricated gDNPs (Supplementary Fig. 2).

gDNPs are highly flexible, compared with traditional rigid depth electrodes, and although flexibility is advantageous once inserted into tissue, this provides a challenge during insertion. To insert these probes we temporarily stiffened the gDNP using SF[18,19]. The stiffening technique (Methods) consisted of a moulding process in which the gDNP is back-coated with SF, allowing the preparation of a rigid shank with a defined shape and thickness. We tuned the thickness of the SF by controlling the mould's trench depth, achieving two typical thicknesses of 80 ± 10 and $150 \pm 12\,\mu m$ (Fig. 1e). The mechanical properties of the SF-coated gDNPs were assessed using a buckling test, in which perpendicularly positioned probes were driven against a flat, hard surface (Fig. 1f). An initial linear increase in force was observed for both coating thicknesses tested, the probes remaining straight before buckling. Continued application of force resulted in buckling and bending, characterized by a peak in the force–displacement curve. The obtained peak forces, $101 \pm 21\,mN$ for the 150-μm-thick SF and $29 \pm 13\,mN$ for the 80-μm-thick SF, are in good agreement with the previously reported values of peak forces for similar SF-coated neural probes[19,31]. We electrically characterized the gDNPs before and after the SF stiffening process, as well as before and after insertion into and removal from an agarose gel brain model. Figure 1g shows the distribution of the normalized g_m as well as V_{RMS} for all 14 transistors in a gDNP, confirming that neither the stiffening process nor insertion in an agarose brain model impairs gDNP performance in terms of transconductance or noise (Supplementary Fig. 3).

Figure 1h depicts video frames of a SF-coated gDNP after insertion (insertion speed $400\,\mu m\,s^{-1}$) in an agarose brain model; the images help to visualize the bending-free insertion of the gDNP shank and the fast water absorption (<10 s) by SF. Moreover, it can be seen that the SF was completely delaminated from the polymeric shank after removal from the agar gel (180 s).

These observations confirm the suitability of the SF back-coating stiffening procedure to enable the flexible gDNPs to reach the target position in a brain-like tissue without bending; the fast dissolution of the shuttle once inserted enables the probe to quickly regain flexibility. This insertion strategy is only suitable for single-time use; for further insertions, the flexible gDNP needs to be recoated. We have verified that the gDNP technology can withstand multiple coating and insertion procedures (Supplementary Fig. 4).

Awake in vivo full-bandwidth recording with gDNPs

We assessed full-bandwidth recording capability by implanting a gDNP into awake, head-fixed mice. The electrophysiological signal measured by the graphene transistors was acquired with a customized electronic system that enables simultaneous recording in two frequency bands with different gains preventing amplifier saturation (Fig. 2a and Methods). gDNPs were implanted in the right hemisphere visual cortex (V1) and lowered until the tip reached hippocampal tissue. Baseline activity was recorded for 10–20 min. To induce network discharges and synchronicity of neuronal bursting, 200 nl of 4-aminopyridine (4-AP, 50 mM), a selective blocker of Kv1 potassium channels[32,33], was focally injected into the cortex adjacent to the gDNP (Fig. 2b).

Full-bandwidth recordings. Figure 2c displays an uninterrupted electrophysiological recording over 2 h (only the uppermost and the lowest channels of the implanted gDNP are displayed); the complete dataset is shown in Supplementary Fig. 5. The ability of the graphene transistors to provide long and stable full-bandwidth recordings without the need for electronic off-set readjustments contrasts the limitation of DC-coupled passive electrodes[34].
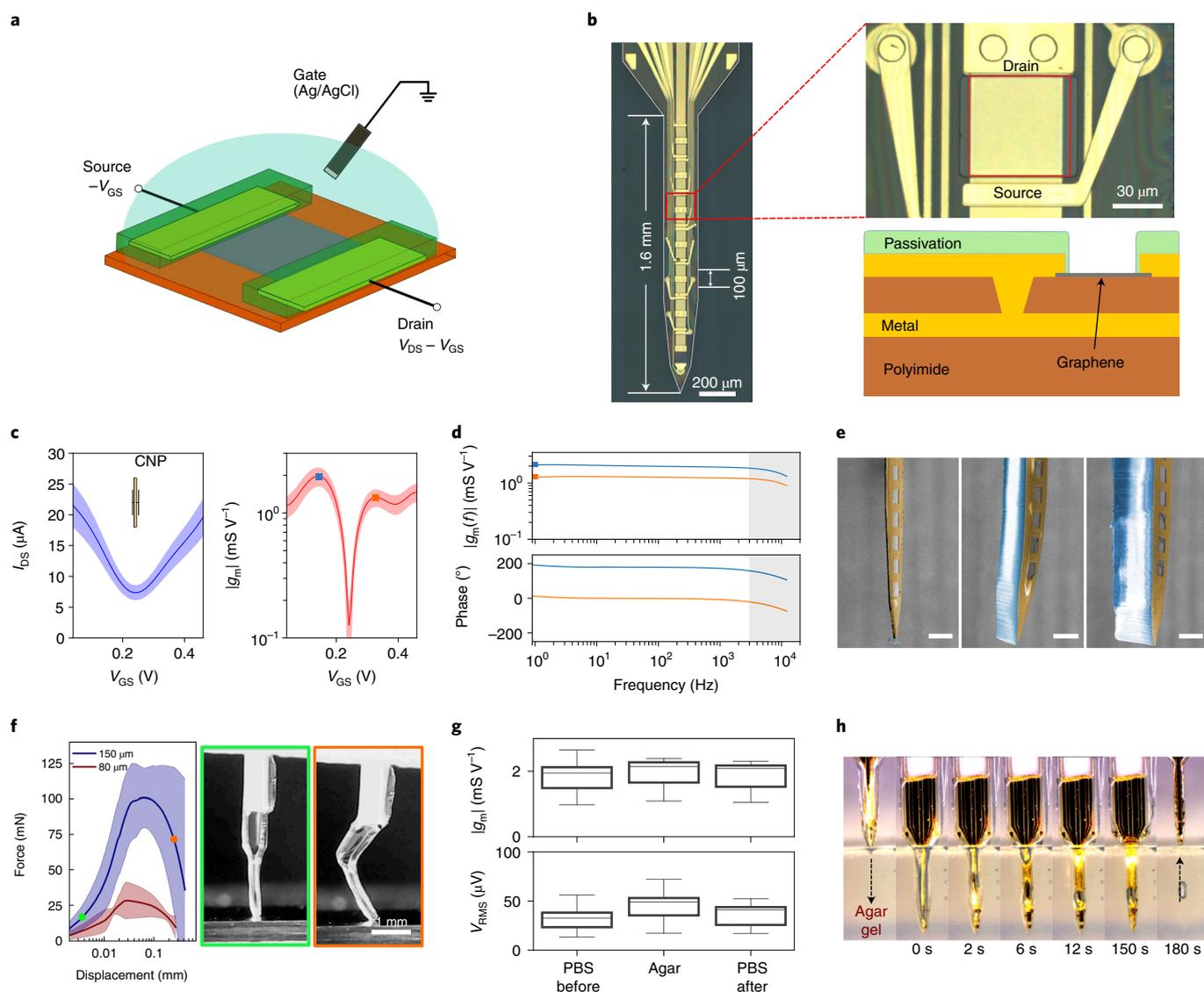
Fig. 1 | Flexible gDNP technology and characterization. a, Schematic of a gSGFET and biasing. **b**, Optical microscope image of a gDNP containing 14 transistors with a pitch of 100 μm on a 200-μm-wide PI shank (left) and a magnification of one gSGFET (top right). The area highlighted in red shows the graphene sensing area (60×60 μm^2) of the transistor. The schematic of the cross-section of one transistor shows the interconnected metal track strategy to reduce the shank width of the gDNP (bottom right). **c**, Electrical characterization of all 14 gSGFETs in a gDNP in a 150 mM saline solution ($V_{DS} = 50$ mV) by measuring I_{DS} and g_m versus V_{GS}. The lines represent mean values and the shadows the standard deviation. **d**, Transconductance spectroscopy of the gSGFET bias at the point of maximum g_m in the electron ($V_{GS} > V_{CNP}$, orange line) and hole ($V_{GS} < V_{CNP}$, blue line) regimes. The squares in **c** (right) are the values of maximum g_m as measured in steady-state mode. The decay observed in the grey shaded areas is due to the filtering of the interfacing electronics. **e**, Coloured scanning electron microscopy images of the gDNP: uncoated (left) and back-coated with ~80-μm-thick (middle) and ~150-μm-thick (right) SF. Scale bars, 100 μm. **f**, Mechanical assessment of the gDNP coated with the two thicknesses of SF showing the averaged compression force versus displacement ($n = 10$ trials; the lines represent the mean, the coloured shadows the standard deviation). The optical images correspond to the two different conditions of the experiment. The image in the green box corresponds to the point marked by the green square in the force–displacement plot, a point before buckling, and the image in the orange box to the point marked by the orange square, representing a point after buckling. **g**, Functionality assessment after insertion in agar. The boxplots ($n = 14$ gGFETs; the median, quartile box and minimum and maximum values are presented) show the distribution of the transconductance (g_m) and V_{RMS} noise level for all gSGFETs in a gDNP measured in phosphate-buffered saline (PBS) solution, inserted and measured inside an agarose gel brain model, and measured in PBS solution after removal from the agarose gel. **h**, Image sequence of a SF-coated gDNP at different timepoints after insertion in the agarose gel brain model, revealing the timeframe of the degradation of the SF coating upon insertion.

The recording shows the full-bandwidth signal (>0.001 Hz) and the signal high-pass (HP)-filtered above 0.5 Hz (which is the expected signal recorded by AC-coupled electrodes)[35]. The recording is broken down into different experimental conditions during the recording: baseline, needle-induced pin-prick SD[36], interictal activity[5] induced by chemoconvulsant drugs and seizures. During baseline recording (Fig. 2c), the lower channels exhibit theta activity, correlated with animal movement, indicating that the gDNP reached the hippocampus, confirmed post hoc by histological analysis of fixed brain sections (Supplementary Fig. 6). After the injection of 4-AP, epileptiform spiking evolved and five seizures (over 60 min) were elicited in this example, one of which was followed by a SD.
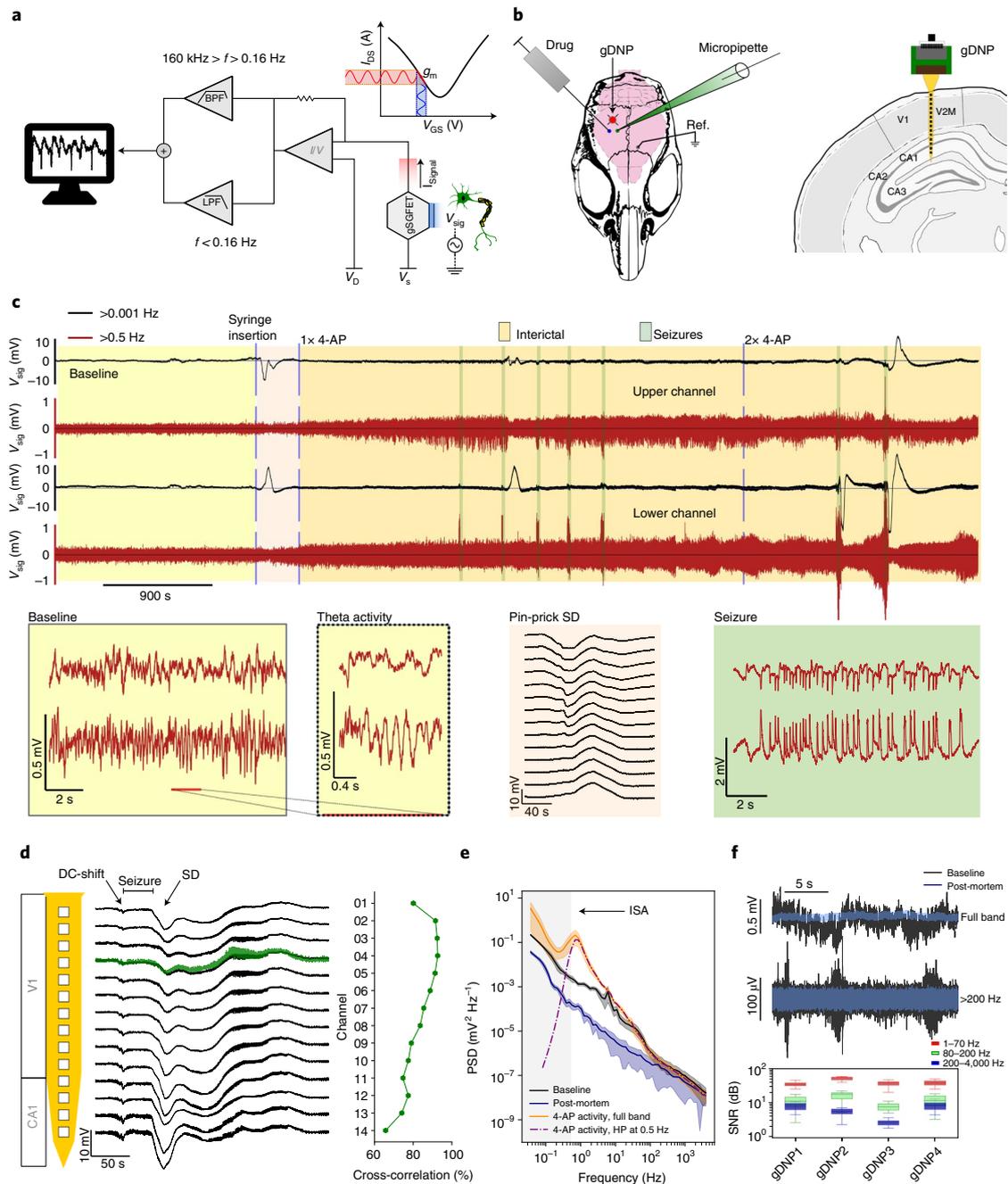
Fig. 2 | Validation of in vivo full-bandwidth recording capabilities of gDNPs. a, Schematic of the recording set-up and concept of a graphene transistor as a transducer for neural recording. V_{sig}, voltage signal; I_{signal}, current signal; V_D, drain voltage; V_S, source voltage. **b**, Schematic of a mouse skull showing the location on the brain of the gDNP, the glass micropipette, the reference electrode (Ref.) and the needle to inject the chemoconvulsant drugs (left). Coronal view of the mouse brain showing the localization of the gDNP (right).V1, primary visual cortex; V2M; medial secondary visual cortex; CA, Cornu Ammonis area of the hippocampus. **c**, Long electrophysiological recording (120 min) of two channels on the gDNP array (the visual cortex (top) and hippocampus (bottom)), showing the full-bandwidth signal (frequency, $f > 0.001\,Hz$) and the HP-filtered signal ($f > 0.5\,Hz$). Baseline activity, pin-prick SD, increased neuronal activity after 4-AP injection and seizures, some of them followed by a SD, are evident. Below, different events are shown in higher resolution: baseline (yellow) revealing theta activity in the lowest channel, profile visualization with recording from all 14 transistors following pin-prick SD (beige) and seizure activity shown for the uppermost and lowest channels of the gDNP (green). **d**, Full-bandwidth recording obtained with the gDNP (black) and glass micropipette (green) after the injection of 4-AP (left). The recording shows the DC-shift concurring with seizure, followed by a SD, recorded by all 14 transistors. The low-frequency cross-correlation analysis of the signals ($<5\,Hz$) from the micropipette and all transistors on the shank shows a very high correlation (right). **e**, Averaged PSD over the electrophysiological recordings of all transistors during baseline, epileptiform activity, epileptiform activity HP-filtered at 0.5 Hz and post-mortem ($n = 14$ gSGFETs; the lines represent the mean, the coloured shadows the standard deviation). The grey area highlights the low-frequency part ($<0.5\,Hz$) usually cut off with conventional AC-coupled recordings. ISA, infraslow activity. **f**, Comparison of baseline activity and post-mortem in one channel of the gDNP for the full-bandwidth signal (top) and HP-filtered signal ($>200\,Hz$; middle). The SNRs of four in vivo experiments performed with four different gDNPs were evaluated (bottom; $n = 14$ gGFETs for each boxplot; the median, quartile box and minimum and maximum whiskers are shown). The SNR was calculated for different frequency bands (low frequency, 1–70 Hz; high frequency, 80–200 Hz; very high frequency, 200–4,000 Hz; see Methods).

A second cortical injection of 4-AP induced two additional seizures, both followed by SDs that were detected first in the hippocampus. In five different mice injected with 4-AP, an average number of 7 ± 3 seizures were recorded in 60 min after drug injection. In this chemoconvulsant model, SDs could be observed initially either in superficial cortical layers or in the hippocampus (Fig. 2c and Supplementary Fig. 7).

The fidelity of the DC-coupled recordings was validated by simultaneous recordings using a solution-filled glass micropipette. Figure 2d shows the full-bandwidth recording obtained with the gDNP and micropipette after the injection of 4-AP. Both recordings reveal DC-shifts preceding seizure, and SD occurring after seizure. The DC-shifts measured by the gDNP have a similar shape, magnitude and temporal duration to the signal recorded by the glass micropipette. A cross-correlation analysis (signal filtered <5 Hz) of the signals recorded by the glass micropipette and the 14 gDNP transistors demonstrated a very high correlation (above 90%) for the channels located at the same cortical depth as the micropipette. The same high correlation was observed during hour-long recordings and for small, sudden DC-shifts (Supplementary Fig. 23).

Assessment of the detection limits of gDNP. Post-mortem recordings were acquired to characterize the electrical noise level of the gDNP in the activity-free brain state and, consequently, to quantify the detection limit of the gDNP. Figure 2e shows the averaged power spectral density (PSD) calculated using the recordings of all channels in a gDNP, obtained from different brain states (baseline, after injection of 4-AP and post-mortem). Compared with the baseline PSD, the large amplitude of the PSD at low frequencies (<1 Hz) after 4-AP injection provides an indication of the interictal and DC-shifts in the brain. We calculated the signal-to-noise ratio (SNR) in three different bands, that is, 1–70, 80–200 and 200–4,000 Hz (Fig. 2f). This analysis shows that the gDNPs are able to record electrophysiological signals in typical bandwidths with a SNR ratio higher than 1 dB.

Electrophysiological recording of characteristic epilepsy biomarkers. Epilepsy alterations of physiological brain activity include interictal spikes, fast activity at hundreds of hertz (such as HFOs) and pre-seizure active DC-shifts. We used two different pro-convulsive drugs (4-AP or picrotoxin (PTX)) to induce and evaluate epileptic activity. Figure 3a shows the interictal activity and associated HFOs (>80 Hz)[22,23] recorded by three of the transistors of a gDNP, each located at a different depth in the mouse brain. Filtering between 80 and 600 Hz revealed layer-specific bursting of HFOs and sharp wave ripples during interictal spikes with characteristic oscillations of 200–300 and 400–600 Hz in the cortical and hippocampal channels, respectively[37] (Supplementary Fig. 8). Entrained interictal epileptiform activity was found in all channels before each seizure. Figure 3b illustrates characteristic examples of sharp wave ripples and HFOs induced by 4-AP and PTX recorded by the lowest channel of the gDNP (hippocampal CA1 region). The HFO and ripple traces shown in Fig. 3b exhibit high-frequency tones up to 600 Hz. The filtered traces (>200 Hz) are compared with the original traces (full bandwidth) for verification of the ripples. The advantage of the gDNPs for monitoring concurrent DC-shifts and high-frequency activity is illustrated in Fig. 3c, which shows an epileptic spike-triggered SD arising from the hippocampus. The layer-dependent silencing of the neural activity by the hippocampal SD is represented in Fig. 3d in terms of the percentage of activity variation. The layer-dependent amplitude of the SD and the following hyperpolarization, also shown in Fig. 3d (more details of this analysis are provided in the Methods and Supplementary Fig. 9), reveal that the silencing of the neural activity in the hippocampus is correlated with the amplitude and subsequent hyperpolarization wave of the SD. The silencing of neural activity in the hippocampus

by the SD is visualized with more clarity in Fig. 3e, where the spectrograms for the uppermost and lowest channels are compared.

DC-shifts are typically associated with seizures[24] and can be differentiated into active shifts that precede the seizure, and passive shifts that follow the intense neuronal firing at seizure onset[38]. For these chemically induced seizures events, we observed that the DC-shift preceded the seizure onset (T_s) by 2–3 s ($n = 4$ seizures; Fig. 3f and Supplementary Fig. 10). Moreover, we observed a layer-dependent amplitude of the DC-shift, with negative amplitudes in the cortical layers (close to the 4-AP injection site) and positive amplitudes recorded in the channels close to the hippocampus (Fig. 3f, bottom left). The spatiotemporal dynamics of the DC-coupled extracellular potential for the pre-ictal to ictal transition is depicted in Fig. 3f (bottom right).

The inversion of DC-shifts can be used to identify current sources and sinks through the cortical laminae. Current source density (CSD) analysis is a technique to identify source activation in a variety of focal neurological disorders, including epilepsy[39,40]. CSD analysis (Methods) of the data in Fig. 3c revealed a large net ionic sink in the hippocampal extracellular space after the seizure, followed by a large source at the beginning of the hyperpolarization wave (Fig. 3g). Enlarging the seizure onset region, four sink and source regions can be identified from the laminae profile. CSD analysis computed with a HP-filtered signal ($0.5\,\text{Hz} < f < 70\,\text{Hz}$) failed to report the ionic sinks preceding and during the seizure in the bottom layers (Fig. 3g, AC-coupled), illustrating the importance of using full-bandwidth recordings for CSD analysis to avoid misinterpretation of the CSD sinks and sources (Supplementary Fig. 11 illustrates additional examples of CSD analyses).

Chronic functional validation and biocompatibility assessment

We implanted gDNPs in the right-hemisphere somatosensory cortex of WAG/Rij rats ($n = 4$), a rodent model of absence epilepsy[20], and obtained chronic full-bandwidth recordings over a 10-week period (Fig. 4a). The WAG/Rij rats exhibited frequent spontaneous SWDs, a characteristic thalamocortical oscillation of 8–10 Hz (ref. [20]; see Methods). Implanted animals were connected 1–2 times per week for tethered recordings (using a commutator to enable free movement of the rats; Fig. 4a and Supplementary Fig. 12).

Transistor curves were measured in each recording session to assess device stability, changes at the device–tissue interface and importantly, to permit selection of an optimal V_{GS} to maximize the SNR, a feature possible with active sensor devices[28]. Figure 4b shows the averaged transfer curves of a gDNP measured over 10 weeks (Supplementary Fig. 13). The stability of the transistors' performance is illustrated in Fig. 4c, which depicts the position of the CNP and the maximum value of g_m over the implantation period. The averaged g_m value remains approximately constant over the whole study. Because g_m is directly related to the tissue–graphene interfacial capacitance and to the carrier mobility in graphene, the stability of g_m strongly suggests little or no variation of these two parameters. The CNP (Fig. 4c) shows a notable shift (200 mV) during the few first days after implantation, and then remains stable for the rest of the experiment. We tentatively attribute the initial shift to the adsorption of negatively charged species, which reduce the intrinsic p-type doping of the graphene transistors[29].

The long-term functionality of the gDNP was assessed by evaluating the quality of the recorded signals over the implantation period using two parameters, normalized SWD power amplitude and the transistor noise (V_{RMS}). For further details, see Methods and Supplementary Figs. 13 and 14. The variation of these parameters over time is shown in Fig. 4d, demonstrating the ability of the implanted devices to monitor seizure activity with high fidelity during the whole implantation period. The slight increase in the normalized SWD activity could result from a strengthened coupling
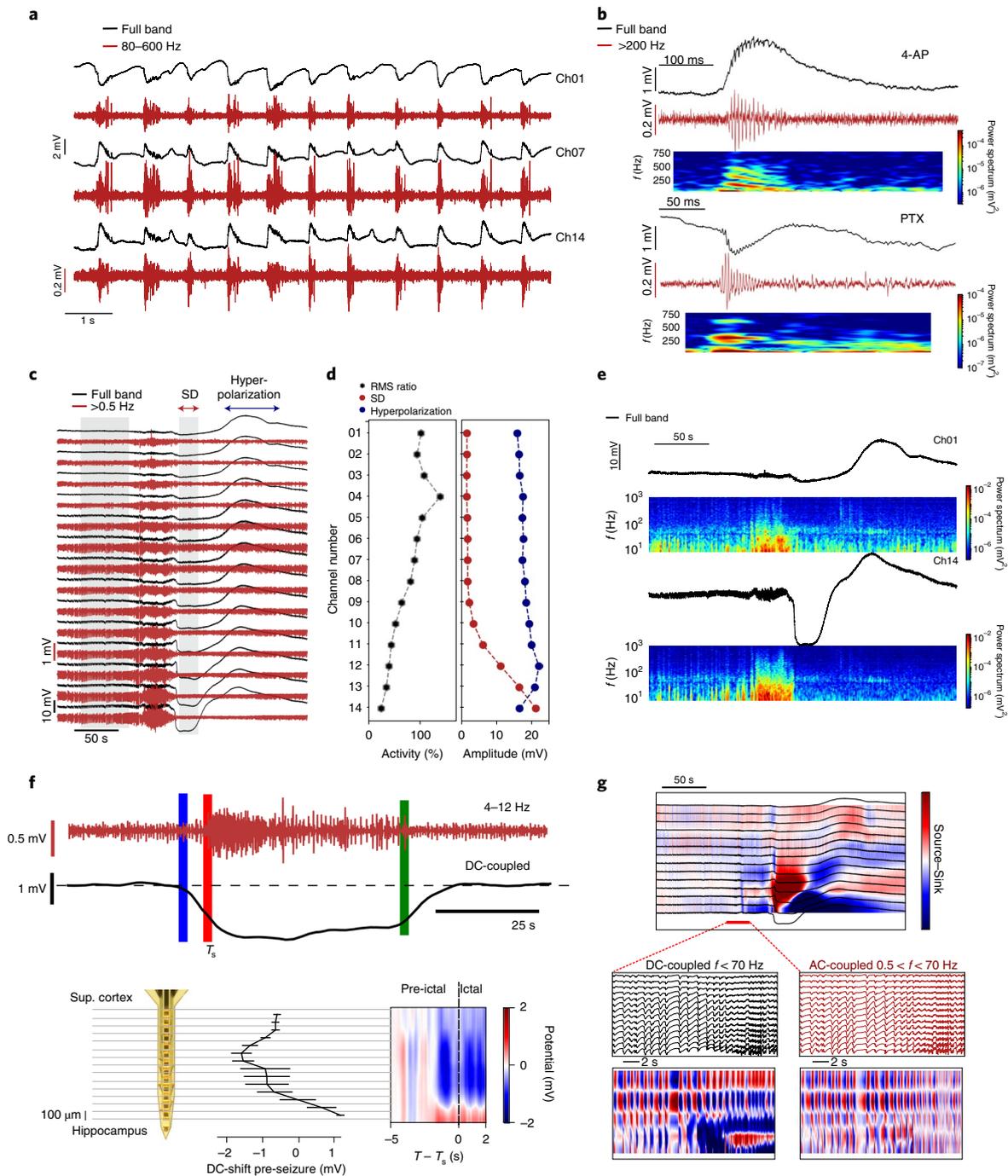
Fig. 3 | Electrophysiological recording of characteristic epilepsy biomarkers. a, Interictal activity in three different channels of a gDNP (Ch01, Ch07 and Ch14), showing full-band and BPF (80–600 Hz) signals. **b**, Sharp wave ripples and HFO recorded in the hippocampus induced by 4-AP and PTX for the full-bandwidth and HP-filtered (>200 Hz) signals. The figure also shows the corresponding spectrograms (range 10–800 Hz). **c**, Electrophysiological full-band recordings and HP-filtered at >0.5 Hz from the cortex (top channel) to the hippocampus (bottom channel) illustrating a SD arising from the hippocampus after a seizure event. **d**, Percentage of neural activity variation calculated for each channel by comparing the activity before and during the SD (corresponding to the grey areas in **c**; left). Absolute amplitudes of the SD and hyperpolarization waves concurrent with the seizure (right). **e**, Hippocampal neural silencing during the SD illustrated by the spectrograms (range 10–1,000 Hz) of the uppermost and lowest channels of the gDNP. **f**, DC-shifts precede seizures at the injection site after administration of 4-AP in awake mice. Representative traces recorded by the gDNP showing a seizure event and the concurrent DC-shift after injection of 4-AP (top). Data are shown for two different frequency bands: DC-coupled (<0.1 Hz) and BPF (4–12 Hz) recordings. T, time. The vertical bars indicate the DC-shift onset (blue), the seizure onset (time T_s, red) and seizure end (green). Depth profile of the peak DC-shift amplitude for each transistor ($n = 4$ seizures; bottom left). The line represents the mean value of the DC-shift and the horizontal bars the standard deviation. Spatiotemporal dynamics of the DC-coupled voltage for the pre-ictal to seizure (ictal) transition (−5 to 2 s; bottom right). The data correspond to the average of $n = 4$ seizures in one mouse (Supplementary Fig. 10). Sup. cortex, superior cortex. **g**, CSD analysis of the low-frequency activity (<70 Hz) corresponding to the recording shown in **c**. Magnifications of the pre-ictal to seizure transition (<70 Hz) are presented, showing dipoles in the different layers of the cortex and hippocampus. The two graphs correspond to the CSD analysis performed with (left) and without (right) the contribution of the DC-coupled signal.
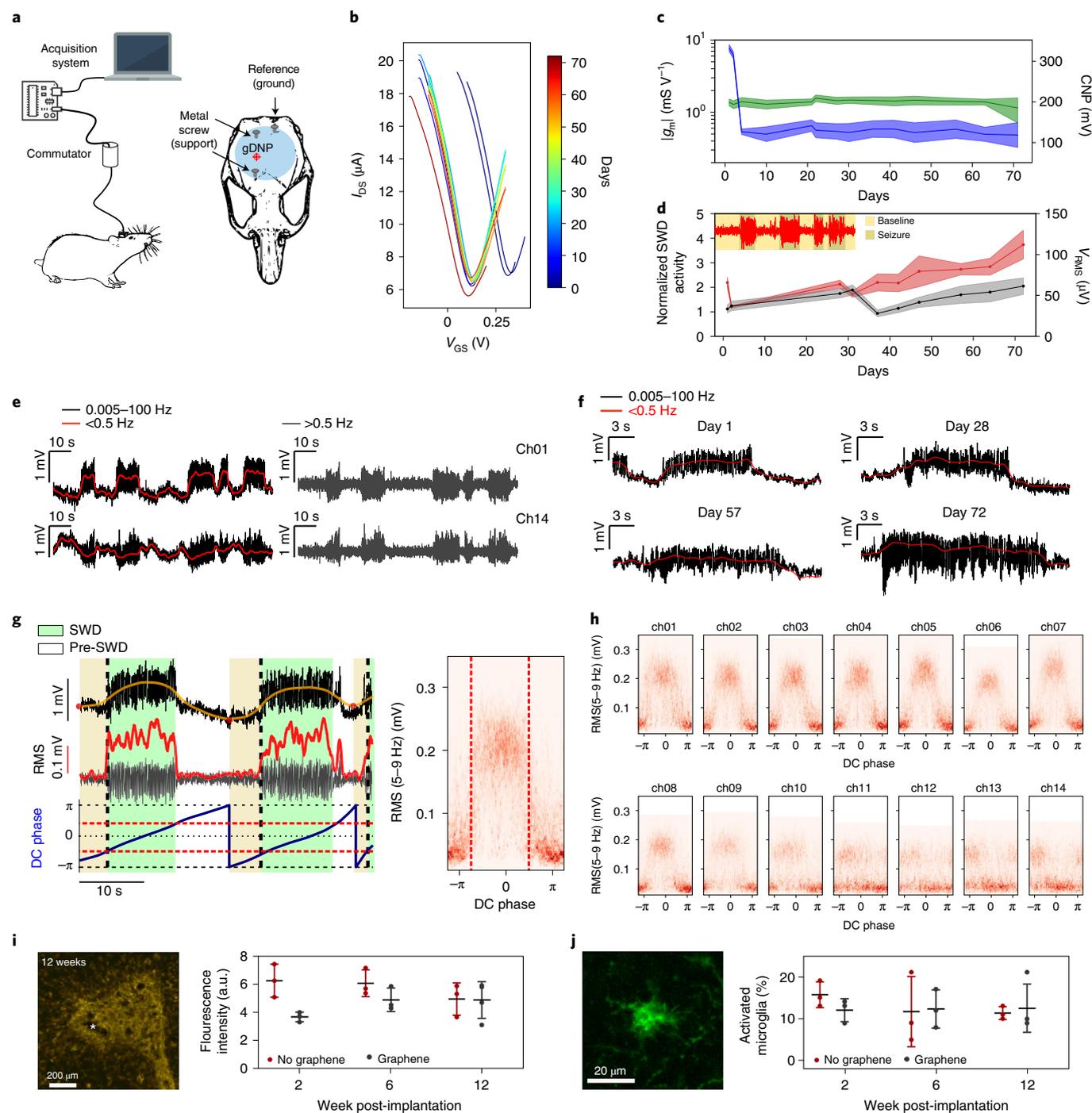
Fig. 4 | Chronic assessment of the stability, functionality and biocompatibility of gDNPs. a, Cartoon of the chronic experimental set-up indicating the approximate location of the gDNP. **b,** Averaged transfer curves ($n=14$ gSGFETs) for one gDNP over the implantation time. **c,** Averaged maximum transconductance (green) and CNP (blue) of the transfer curves shown in **b** ($n=14$ gSGFETs; the lines represent the mean, the coloured shadows the standard deviation). **d,** Normalized SWD activity (red), calculated as the ratio of the SWD and baseline activity, and average V_{RMS} noise (black) of all channels over the implantation period ($n=14$ gSGFETs; the lines represent the mean, the coloured shadows the standard deviation). **e,** SWDs in the uppermost and lowest channels. The DC potential ($<0.5\,Hz$) overlaps the 0.005–100 Hz signal; the signal filtered above 0.5 Hz is also shown. **f,** SWD events in the same channel at days 1, 28, 57 and 72. **g,** Amplitude–phase correlation between ISO and SWD (left). The recording (Ch02, black, 0.01–100 Hz) shows two SWD events (green shadow) with ISO (yellow, 0.01–0.1 Hz; top), RMS (red, 5–9 Hz) with HP filtering (grey, >1 Hz; middle) and the ISO phase (blue, 0.01–0.1 Hz; bottom). The red dotted lines mark the SWD ISO phase. Density distribution of the ISO phase and SWD RMS in the same channel is also shown (right), distinguishing low density (white) and high density (red) regions. **h,** Density distribution for all channels. **i,j,** Chronic biocompatibility of gDNPs in Sprague Dawley rats ($n=20$) at time points of 2, 6 and 12 weeks ($n=6$ for each time point), analysing for astrocyte cells (**i**) and microglia activation (**j**). The fluorescent image of GFAP in **i** is a measure of positive astrocyte cells, in the area of insertion, at 12 weeks (the star indicates the insertion point). The evolution of fluorescence intensity (150 µm from the probe site) obtained for probes with and without graphene is shown. Example fluorescent image of activated microglia (**j**). The evolution of activated microglia (0.7 mm² around the insertion site) is shown in **j** for both types of probes. The data are presented as mean values with standard deviation.

between neural tissue and the gDNP or from an increase in the seizure power and duration as the animal ages[41].

Correlation between SWDs and infraslow oscillations. The WAG/Rij rat chronic model of absence epilepsy offers the possibility to investigate correlations between infraslow oscillations (ISOs) and SWD events[42]. Owing to the full-bandwidth capability of the gDNP, we were able to observe these correlations as well as a dipole across the neocortex upper and lower layers. Figure 4e shows the uppermost and lowest channels having opposite phases during each SWD (Supplementary Fig. 15). The information contained in the DC-shift is lost after application of a HP filter (>0.5 Hz), as typically used with conventional AC-coupled microelectrodes (Fig. 4e, right). This observation persists over the implantation period, as shown in Fig. 4f. To further evaluate the relation of ISOs and SWDs, we calculated the phase of the signals (limited to the 0.01–0.1 Hz band) and the power of the neural activity associated with the SWDs (5–9 Hz). Figure 4g displays the full band and the ISO component (0.001–0.1 Hz) of the signal recorded from one of the upper channels, together with the RMS of the SWD signal (5–9 Hz) and the ISO phase. Prior to the SWD events, whose onset is marked by the abrupt increase of the SWD RMS, the ISO phase is consistently observed to change (Supplementary Figs. 15 and 16). The correlation between the ISO phase and the SWD can be better illustrated by the joint probability distribution plot (Fig. 4g, right) obtained from a long recording (1,600 s, >35 SWDs; see Methods). Figure 4h depicts the correlation between the ISO phase and the RMS of the SWDs for each channel, revealing an inversion in the lower layer of the neocortex (Supplementary Fig. 16). To further confirm the capability to observe these ISOs preceding the seizure events, we calculated the depth profile of the DC-coupled signal (averaged for $n = 9$ SWD events) in a timeframe around the start of the SWDs. Preceding the SWD (with its characteristic positive DC-shift) by a couple of seconds, a small negative DC-shift was observed at superficial to medial layers (Supplementary Fig. 17).

This correlation between ISO and SWD was also observed in the other implanted WAG/Rij rats ($n = 4$; Supplementary Fig. 18).

Chronic biocompatibility of implanted gDNP. We also conducted an extensive chronic biocompatibility study to assess any potential neuroinflammation caused by the invasive nature of the penetrating neural probes, the presence of CVD graphene or by the release of SF following implantation. Neural probes with or without graphene at the recording sites were implanted in adult, male Sprague Dawley rats ($n = 20$). Histological and immunohistochemical studies were conducted at 2, 6 and 12 weeks post-implantation and compared with the contralateral hemisphere without device implantation (Supplementary Figs. 19 and 20). An additional small cohort of animals ($n = 3$) were implanted with commercially available rigid depth neural probes with similar dimensions (NeuroNexus, Supplementary Fig. 19). Figure 4i shows a fluorescence image of glial fibrillary acidic protein (GFAP) immunostaining (positive marker for astrocyte cells) in the area of insertion 12 weeks post-implantation (brain sections at 800 μm from the pia). There was no significant difference in the number and morphology phenotype of astrocyte cells (typically associated with inflammation) in the area directly surrounding the implanted probe site, or on comparison between probes with or without graphene (Fig. 4i, right). No significant difference was observed at 2, 6 and 12 weeks post-implantation, and values are in the same range as in the contralateral hemisphere where no probe was inserted (Supplementary Fig. 19). The activation state of microglia, assessed by morphological analysis of cells stained for ionized calcium binding adaptor molecule 1, showed no significant increase in the abundance of activated microglia present in the area surrounding the implantation site (Fig. 4j). Additional immunohistochemical analysis showed no sign of an inflammatory response

over the 12-week period for either device used, comparable to commercially available rigid probes (Supplementary Fig. 19). Recently published biocompatibility data from some of our laboratories using flexible gFET devices designed with large graphene surface areas implanted epicortically also showed no significant adverse tissue response chronically[43]. Altogether, the chronic biocompatibility study reported here indicates that gDNPs are suitable for deep brain structure chronic implantations, inducing no significant tissue damage nor neuroinflammatory responses.

Outlook

We have demonstrated in this study the capability of gDNPs based on linear arrays of gSGFETs to record electrophysiological brain activity in a wide temporal range, with fidelity similar to solution-filled glass micropipettes but with superior spatial sampling. The gDNP is a novel technology that allows concurrent recordings of DC-shifts, ISOs and HFOs in preclinical epileptic models through the cortex laminae to upper hippocampal layers.

Together with the validation of the chronic functionality of implanted gDNPs and their biocompatibility, our work underlines the very distinct advantages of this technology for in vivo epilepsy research. In particular, the gDNPs have allowed us to reveal in rodent models of drug-induced seizures and chronic epilepsy[20] associations between DC-shifts (including ictal baseline shifts and SDs[24–26,44,45]) and higher-frequency activity (including SWDs[21] and HFOs[22,23]).

The reliability, stability and high fidelity of the recordings observed in this work suggest that this technology could be eventually used to record clinically relevant electrophysiological biomarkers. In this respect, we envision that clinical development of this technology could be directed towards neural probes capable of simultaneous high-quality wide-band (DC to HFO) recordings from multiple brain regions during pre-surgical monitoring. Moreover, this technology could be applied combining depth and subdural gSGFET arrays capable of stable DC-coupled recordings with high spatial resolution, which will offer advantages over current technologies for epilepsy and neurocritical care[11,46]. In particular, it is expected that this technology can help improve the identification of seizure onset zones and ultimately surgical outcome[5]. Currently, long-term seizure freedom after surgery is only around ~50% (ref. [47]); thus, improvements in a technology that more precisely defines surgical margins is warranted. The few studies that have investigated DC-shifts report that these signals co-localize with seizure onset zones and are more spatially restricted than conventional electroencephalogram (EEG) recordings[48]. Therefore, routine inclusion of accurate DC-coupled recordings in surgical monitoring, which can be enabled by the technology described in this work, could result in less extensive, yet more effective surgical resections[9]. Beyond its use for epilepsy research, we envision that this technology can be applied to advance our understanding of other neurological diseases associated with SD, including traumatic brain injury, stroke and migraine[49].

Online content

Any methods, additional references, Nature Research reporting summaries, source data, extended data, supplementary information, acknowledgements, peer review information; details of author contributions and competing interests; and statements of data and code availability are available at https://doi.org/10.1038/s41565-021-01041-9.

References

1. Perucca, P., Dubeau, F. & Gotman, J. Intracranial electroencephalographic seizure-onset patterns: effect of underlying pathology. *Brain* **137**, 183–196 (2014).

2. Modur, P. N. High frequency oscillations and infraslow activity in epilepsy. *Ann. Indian Acad. Neurol.* **17**, S99–S106 (2014).

3. Revankar, G. S. et al. in *Seizures in Critical Care: A Guide to Diagnosis and Therapeutics* (eds Varelas, P. N. and Claassen, J.) 77–90 (Humana Press, 2017); https://doi.org/10.1007/978-3-319-49557-6_5

4. Dreier, J. P. The role of spreading depression, spreading depolarization and spreading ischemia in neurological disease. *Nat. Med.* **17**, 439–447 (2011).

5. Staba, R. J., Stead, M. & Worrell, G. A. Electrophysiological biomarkers of epilepsy. *Neurotherapeutics* **11**, 334–346 (2014).

6. Dell, K. L., Cook, M. J. & Maturana, M. I. Deep brain stimulation for epilepsy: biomarkers for optimization. *Curr. Treat. Options Neurol.* **21**, 47 (2019).

7. Kuhlmann, L., Lehnertz, K., Richardson, M. P., Schelter, B. & Zaveri, H. P. Seizure prediction—ready for a new era. *Nat. Rev. Neurol.* **14**, 618–630 (2018).

8. Chari, A., Thornton, R. C., Tisdall, M. M. & Scott, R. C. Microelectrode recordings in human epilepsy: a case for clinical translation. *Brain Commun.* **2**, fcaa082 (2020).

9. Lee, S. et al. DC shifts, high frequency oscillations, ripples and fast ripples in relation to the seizure onset zone. *Seizure* **77**, 52–58 (2020).

10. Li, C. et al. Evaluation of microelectrode materials for direct-current electrocorticography. *J. Neural Eng.* **13**, 16008 (2015).

11. Hartings, J. A. How slow can you go? *Nat. Mater.* **18**, 194–196 (2019).

12. Major, S., Gajovic-Eichelmann, N., Woitzik, J. & Dreier, J. P. Oxygen-induced and pH-induced direct current artifacts on invasive platinum/iridium electrodes for electrocorticography. *Neurocrit. Care* **35**, 146–159 (2021).

13. Khodagholy, D. et al. In vivo recordings of brain activity using organic transistors. *Nat. Commun.* **4**, 1575 (2013).

14. Kostarelos, K., Vincent, M., Hebert, C. & Garrido, J. A. Graphene in the design and engineering of next-generation neural interfaces. *Adv. Mater.* **29**, 1700909 (2017).

15. Blaschke, B. M. et al. Mapping brain activity with flexible graphene micro-transistors. *2D Mater.* **4**, 025040 (2017).

16. Hébert, C. et al. Flexible graphene solution-gated field-effect transistors: efficient transducers for micro-electrocorticography. *Adv. Funct. Mater.* **28**, 1703976 (2017).

17. Masvidal-Codina, E. et al. High-resolution mapping of infraslow cortical brain activity enabled by graphene microtransistors. *Nat. Mater.* **18**, 280–288 (2019).

18. Weltman, A., Yoo, J. & Meng, E. Flexible, penetrating brain probes enabled by advances in polymer microfabrication. *Micromachines* **7**, 180 (2016).

19. Tien, L. W. et al. Silk as a multifunctional biomaterial substrate for reduced glial scarring around brain-penetrating electrodes. *Adv. Funct. Mater.* **23**, 3185–3193 (2013).

20. Coenen, A. M. L. & Van Luijtelaar, E. L. J. M. Genetic animal models for absence epilepsy: a review of the WAG/Rij strain of rats. *Behav. Genet.* **33**, 635–655 (2003).

21. Terlau, J. et al. Spike-wave discharges in absence epilepsy: segregation of electrographic components reveals distinct pathways of seizure activity. *J. Physiol.* https://doi.org/10.1113/JP279483 (2020).

22. Zijlmans, M. et al. High-frequency oscillations as a new biomarker in epilepsy. *Ann. Neurol.* **71**, 169–178 (2012).

23. Jacobs, J. et al. High-frequency oscillations (HFOs) in clinical epilepsy. *Prog. Neurobiol.* **98**, 302–315 (2012).

24. Ikeda, A. et al. Focal ictal direct current shifts in human epilepsy as studied by subdural and scalp recording. *Brain* **122**, 827–838 (1999).

25. Wu, S. et al. Role of ictal baseline shifts and ictal high-frequency oscillations in stereo-electroencephalography analysis of mesial temporal lobe seizures. *Epilepsia* **55**, 690–698 (2014).

26. Vanhatalo, S. et al. Very slow EEG responses lateralize temporal lobe seizures: an evaluation of non-invasive DC-EEG. *Neurology* **60**, 1098–1104 (2003).

27. Duan, X. et al. Intracellular recordings of action potentials by an extracellular nanoscale field-effect transistor. *Nat. Nanotechnol.* **7**, 174–179 (2012).

28. Hess, L. H. Graphene transistors for biosensing and bioelectronics. *Proc. IEEE* **101**, 1780–1792 (2013).

29. Hess, L. H. et al. High-transconductance graphene solution-gated field effect transistors. *Appl. Phys. Lett.* **99**, 033503 (2011).

30. Garcia-Cortadella, R. et al. Distortion-free sensing of neural activity using graphene transistors. *Small* **16**, 1906640 (2020).

31. Lecomte, A. et al. Silk and PEG as means to stiffen a parylene probe for insertion in the brain: toward a double time-scale tool for local drug delivery. *J. Micromech. Microeng.* **25**, 125003 (2015).

32. Fueta, Y. & Avoli, M. Effects of antiepileptic drugs on 4-aminopyridine-induced epileptiform activity in young and adult rat hippocampus. *Epilepsy Res.* **12**, 207–215 (1992).

33. Padmanabhan, K. & Urban, N. N. Disrupting information coding via block of 4-AP-sensitive potassium channels. *J. Neurophysiol.* **112**, 1054–1066 (2014).

34. Zakharov, A., Chernova, K., Burkhanova, G., Holmes, G. L. & Khazipov, R. Segregation of seizures and spreading depolarization across cortical layers. *Epilepsia* **60**, 2386–2397 (2019).

35. Hartings, J. A. et al. Direct current electrocorticography for clinical neuromonitoring of spreading depolarizations. *J. Cereb. Blood Flow Metab.* **37**, 1857–1870 (2017).

36. Harriott, A. M., Takizawa, T., Chung, D. Y. & Chen, S. P. Spreading depression as a preclinical model of migraine. *J. Headache Pain* **20**, 45 (2019).

37. Buzsáki, G. & Lopes da Silva, F. L High frequency oscillations in the intact brain. *Prog. Neurobiol.* **98**, 241–249 (2012).

38. Ikeda, A. et al. Active direct current (DC) shifts an "Red slow": two new concepts for seizure mechanisms and identification of the epileptogenic zone. *Neurosci. Res.* **156**, 95–101 (2020).

39. Kamarajan, C., Pandey, A. K., Chorlian, D. B. & Porjesz, B. The use of current source density as electrophysiological correlates in neuropsychiatric disorders: a review of human studies. *Int. J. Psychophysiol.* **97**, 310–322 (2015).

40. Flynn, S. P., Barrier, S., Scott, R. C., Lenck-Santini, P. P. & Holmes, G. L. Status epilepticus induced spontaneous dentate gyrus spikes: *in vivo* current source density analysis. *PLoS ONE* **10**, e0132630 (2015).

41. Coenen, A. M. L. & Van Luijtelaar, E. L. J. M. The WAG/Rij rat model for absence epilepsy: age and sex factors. *Epilepsy Res.* **1**, 297–301 (1987).

42. Orlowska-Feuer, P. et al. Infra-slow modulation of fast beta/gamma oscillations in the mouse visual system. *J. Physiol.* **599**, 1631–1650 (2021).

43. Garcia-Cortadella, R. et al. Graphene active sensor arrays for long-term and wireless mapping of wide frequency band epicortical brain activity. *Nat. Commun.* **12**, 211 (2021).

44. Bahari, F. et al. Seizure-associated spreading depression is a major feature of ictal events in two animal models of chronic epilepsy. Preprint at *bioRxiv* https://doi.org/10.1101/455519 (2020).

45. Dreier, J. P. et al. Spreading convulsions, spreading depolarization and epileptogenesis in human cerebral cortex. *Brain* **135**, 259–275 (2012).

46. Dreier, J. P. et al. Recording, analysis, and interpretation of spreading depolarizations in neurointensive care: review and recommendations of the COSBID research group. *J. Cereb. Blood Flow Metab.* **37**, 1595–1625 (2017).

47. De Tisi, J. et al. The long-term outcome of adult epilepsy surgery, patterns of seizure remission, and relapse: a cohort study. *Lancet* **378**, 1388–1395 (2011).

48. Kanazawa, K. et al. Intracranially recorded ictal direct current shifts may precede high frequency oscillations in human epilepsy. *Clin. Neurophysiol.* **126**, 47–59 (2015).

49. Lauritzen, M. et al. Clinical relevance of cortical spreading depression in neurological disorders: migraine, malignant stroke, subarachnoid and intracranial hemorrhage, and traumatic brain injury. *J. Cereb. Blood Flow Metab.* **31**, 17–35 (2011).

Methods

Microfabrication of flexible gDNPs. Flexible neural probes were fabricated using standard microelectronic fabrication technology on a rigid 10-cm sacrificial Si/SiO$_2$ wafer. A 10-μm-thick PI (PI-2611, HD MicroSystems) layer was spin-coated and cured at 350 °C in a N$_2$ atmosphere. To reduce the shank width of the depth neural probes, we used a two-metal-level strategy in which the metal tracks, separated by PI, are interconnected by via holes. After evaporation and definition (by lift off) of a first metal layer of Ti/Au (10/100 nm), a 3-μm-thick PI layer was spin-coated and cured. A protective mask of Al (200 nm) was used to etch the second PI layer using oxygen plasma and form the via holes. On top of the via holes a second metal layer of Ti/Au (10/100 nm) was applied to interconnect the two metal layers. CVD graphene was transferred onto the patterned wafer as described in the Supplementary Information Methods. The graphene active areas were defined by oxygen-based reactive ion etching. A sandwich-like contact strategy was used to improve the contact at the drain and source terminals; the top metal structure consisted of Ni/Au (20/200 nm). For passivation, a 2-μm-thick chemically resistant polymer was deposited (SU8-2005 MicroChem) with open windows in the channel region. Finally, the gDNP structure was defined in a deep reactive ion etching process using a thick AZ9260 positive photoresist (Clariant) as etching mask. The PI probes were then released from the SiO$_2$ wafer and placed in a zero insertion force connector to interface our custom electronics. The transconductance of the flexible gSGEFTs could be improved by ultraviolet ozone cleaning of the contact region at the graphene–metal interface, as recently demonstrated for flexible graphene neural sensors[50]. For CVD graphene growth, transfer and its characterization we refer to the Supplementary Information.

Characterization of gDNPs in saline. The gSGFETs on the neural probes were characterized in PBS solution (150 mM). Drain–source currents (I_{DS}) were measured varying the gate–source voltage (V_{GS}) versus a Ag/AgCl reference electrode, which was set to ground. Steady state was ensured by acquiring the current only after its time derivative was below a threshold (10^{-7} A s^{-1}). The detection limit of the gSGFET was assessed by measuring the PSD of the DC current at each polarization point V_{GS}. Integrating the PSD over the frequencies of interest (1 Hz–2 kHz) and using the transconductance allowed us to calculate V_{RMS}. The noise measurement was performed in a Faraday cage, with DC-batteries powering the amplifiers, to reduce any 50 Hz coupling or pick-up noise. Additionally, the frequency response of the device's transconductance was measured by applying a sum of sinusoidal signals to the electrolyte solution through the reference electrode and by measuring the modulation of the drain current. The acquired signals were split into two bands: low frequencies (~0–10 Hz), at which the drain–source current was simultaneously acquired for all transistors in an array, and higher frequencies (10 Hz–30 kHz), at which each transistor was recorded individually.

Back-coating of gDNP with silk fibroin. Compared with other natural biopolymers, SF offers excellent mechanical properties, extremely good biocompatibility, biodegradability and the versatility of structural readjustments[51–53]. Further, the byproducts of SF degradation by enzymes (for example, proteases) have low antigenicity and non-inflammatory characteristics[54,55]. Temporary stiffening of the gDNPs with SF was achieved using a microstructured polydimethylsiloxane (PDMS) mould with the shape of the neural probes. To fabricate the moulds, PDMS was cast on a standard 4-inch silicon wafer with prepatterned 100- and 200-μm-thick SU8 (SU8-2050) epoxy resin. The back-coating procedure was as follows: first, the probe was placed in the mould trench filled previously with water, with the transistor side facing down. Through surface tension effects, the probe self-aligned in the mould. After evaporation of the water, SF (Silk, Fibroin Solution 50 mg ml^{-1}, Sigma Aldrich) was applied through a syringe to the mould's trench. We double-coated the shank in drying intervals of 20 min and then slowly increased the temperature on a hotplate to 80 °C, leaving the SF to cure for 90 min. To have a delayed dissolution time compared with the SF curing time at room temperature, we increased the duration of the water annealing step. After curing, the coated probe can be easily removed from the PDMS mould (Supplementary Fig. 3). In all the in vivo experiments presented here, we implanted the flexible gDNPs with a 150-μm-thick SF back-coating.

Assessment of mechanical properties of the stiffened gDNPs. Standard compression tests against a hard Si substrate were performed to assess the mechanical properties of our SF-coated probes. Buckling experiments were carried out in a UMIS nanoindenter (Fischer-Cripps Laboratories). A custom clamp was fabricated to fix the probes at the end of the indenter shaft, which, in turn, was connected to an actuator and load cell. Buckling tests were carried out at a loading rate of 8.8 mN s^{-1}. Once the indenter detected noticeable buckling the test was automatically stopped. The maximum applied load that the indenter can apply is 500 mN. Applied force versus displacement was measured until the probe started to buckle and eventually broke down. We additionally measured the Young's modulus of the SF cured at 80 °C by nanoindentation tests. SF was dropcast on a 2 × 2 cm^2 Si chip and cured. Indentation was measured using an NHT2 Nanoindentation Tester (Anton-Paar) equipped with a Berkovich pyramidal-shaped diamond tip. A maximum applied load of 5 mN was applied with a loading segment of 30 s

followed by a load holding segment of 10 s and an unloading segment of 30 s. The hardness and reduced Young's modulus are reported as average values of at least 20 indentations, performed on top of each sample (in the central region). Young's modulus values in the range of 10 GPa were measured for SF cured at 80 °C (Supplementary Fig. 22).

Electronics for in vivo recordings with gDNPs. The experimental set-up used to perform the in vivo recordings provided V_S and V_D bias control and current-to-voltage conversion for up to 16 channels (g.RAPHENE, g.tec medical engineering). The instrumentation split the recorded signals into two bands with different gains: low-pass filtered (LPF; <0.16 Hz, 10^4 gain) and band-pass filtered (BPF; 0.16 Hz < f < 160 kHz, 10^6 gain). Two custom Simulink models were used (1) to generate the transfer curve of the microtransistors once inserted and at the end of the experiment, and (2) to set the V_S and V_D bias and acquire the recorded signals. Signals were sampled at 9.6 and 19 kHz, depending on the type of experiment (Supplementary Table 1).

Ethical approval and animal handling for acute and chronic experiments. Animal experiments were conducted in accordance with the United Kingdom Animal (Scientific Procedures) Act 1986, and approved by the Animals in Scientific Research Unit at the Home Office (licence PPL70-13691). C57BL/ mice were bred (2–4-month-old males), whereas WAG rats were imported (Charles River, 6–9 months of age). Animals were housed in a 12 h/12 h dark/light cycle, and food and water were given ad libitum. The animals were group-housed prior to headbar surgery, but after this, animals were individually housed.

Acute preparation surgeries for headbar attachment and craniotomy. For both surgeries, aseptic techniques were used with mice anaesthetized using isoflurane (988–3245, Henry Schein) and placed in a stereotaxic frame (David Kopf Instruments). Viscotears were applied (Bausch + Lomb) and pain relief, which consisted of subcutaneous bupenorphine (0.5 mg per kg mouse (hereafter denoted mg kg^{-1} mouse); Ceva) and metacam (15 mg kg^{-1} mouse; Boehringer Ingelheim), was injected. Saline was administered just before recovery or every 45 min depending on the length of surgery. To apply the headbars for the Neurotar system, the skin on the top of the head was cut to expose the skull. The skull was cleaned and dried, which enabled drilling (RA1 008, Henry Schein) of a small hole in the left-hand visual cortex for a metal support screw (00-96 × 3-32, Plastics One). The headplate (Model 9, Neurotar) was firmly attached using vetbond (1469SB, 3M) and strengthened using dental cement before the exposed skull was covered with Kwik-Cast (WPI). Mice were checked daily to ensure recovery. After at least 5 days of recovery, habituation was performed by placing the mouse in the Neurotar frame for increasing periods of time (15–60 min) over several days. On the day of recording, a craniotomy was performed. Under isoflurane anaesthesia, with administration of pain medication and intramuscular dexamethasone (1 mg per kg of mouse, intramuscular; 7247104, MSD Animal Health), two areas were exposed. A large (2 × 2 mm^2) craniotomy was performed over the somatosensory and visual cortex on the right-hand side and a small drill hole over the motor cortex on the left-hand side. Cold Cortex-buffered saline was continually applied to the craniotomies. After completion, the exposed dura was covered with Cortex-buffered saline, sterilized Sylgard (~200-μm thick) and a Kwik-Cast layer. After ~2 h, the animal was moved to the Neurotar frame and the craniotomies were exposed by removal of the Kwik-Cast and Sylguard layers. The gDNP was carefully connected to a printed circuit board (PCB) and lowered using a micromanipulator to just above the dura over the visual cortex. The dura was gently pierced using either microdissection scissors or a 26-gauge needle and the gDNP lowered ~2 mm into the brain. A reference wire (Ag/AgCl$_2$) was placed in the ipsilateral motor cortex and g.tec hardware (see the section Electronics for in vivo recordings with gDNPs) was used to generate the transfer curve to determine the optimal V_{GS} and initiate recordings (Supplementary Fig. 4). Chemoconvulsant was injected into the brain using a Nanofil injection system (WPI). At the end of the experiment, sodium pentobarbital was administered intraperitoneally.

Recording with solution-filled glass micropipette. Borosilicate capillary tubes (outer diameter 1.50 mm, inner diameter 0.86 mm; Warner Instruments) were pulled using a horizontal puller (Sutter Instruments P-97, resistance of 3–5 MΩ), filled with artificial cerebral spinal fluid (119 mM NaCl, 2.5 mM KCl, 2.5 mM CaCl$_2$, 1.3 mM MgSO$_4$, 1.25 mM NaH$_2$PO$_4$, 25 mM NaHCO$_3$ and 10 mM glucose) and attached to an CV-7B headstage (Axon Instruments). A micromanipulator (MM3301, WPI) was used to position the pipette above the cortical surface before insertion approximately 400 μm into the cortex. The headstage was provided with the same reference as the gDNP, a chlorinated silver wire touching the ipsilateral motor cortex. The headstage was connected to a Multiclamp 700B amplifier (Axon Instruments) operating in current clamp mode. Analogue–digital conversion and transistor–transistor logic pulse delivery for temporal synchronization was achieved using a Micro1401 MkII unit (CED). Data were acquired by WINEDR sampling at 20 kHz with a 4 kHz Bessel filter.

Chronic preparation surgery and recording. First, the gDNP was coated with fibroin, as described above, to aid insertion. The rat was anaesthetized to a surgical

depth using Isoflurane. After placement in a stereotaxic frame, Viscotears were applied and pain medication, which consisted of bupenorphine (0.15 mg kg⁻¹ mouse, subcutaneous; Ceva) and metacam (4.5 mg kg⁻¹ mouse, subcutaneous; Boehringer Ingelheim), was injected. The skull was cleaned and dried. Small burr holes (~1 mm) were drilled at four positions: (1) the somatosensory cortex for gDNP (as the perioral somatosensory cortex is the focal area for SWDs[56]), (2) the contralateral cerebellum for a reference Ag/AgCl wire held in place by a nylon screw, (3) the motor cortex, ipsilateral, for a support screw and (4) the visual cortex, ipsilateral, for a support screw. The metal screws were inserted and provided structural support for the dental cement. Next, the gDNP and reference wire were inserted, and a DC characterization curve confirmed that the transistors were performing optimally. Dental cement, mixed with vetbond, was applied around the PCB for support. Animals were weighed daily and their physiology was monitored to ensure a full recovery. For recording, animals were anaesthesia-free and moving, with the PCB interface on the head connected to an Omnetics cable (A79635, Omnetics) that interfaced with the g.tec recording hardware as described above. After allowing ~5 min for settling, a DC characterization curve was recorded to allow accurate calibration of the gSGFETs. A script was used to calculate the optimal V_{GS} based on the transfer curves. Recordings were performed for ~10–60 min twice a week for 10 weeks. After recording, the Omnetics wire was disconnected and a protective cap was applied.

WAG/Rij strain of rats. WAG/Rij rats were used as a model of absence epilepsy. Spike-wave activity in the cortical EEG of adult WAG/Rij rats has a frequency of 7–10 Hz and can last from just a few, to up to 40 s in duration. From an age of 6 months, WAG/Rij rats display several hundred SWDs a day[20]. In addition to electrophysiological signs, mild behavioural phenotypes concurrent with SWD similar to human absence epilepsy are displayed. These include facial myoclonic jerks, twitching, accelerated breathing, head tilting and eye blinking. Drugs prescribed for human absence epilepsy suppress SWDs in WAG/Rij rats, and these rats have been used to predict the action of antiepileptic medication and other experimental treatments[57].

Data analysis. All electrophysiological data were analysed using Python v.3.7 packages (Matplotlib, Numpy, Neo and Elephant) and the custom library PhyREC (https://github.com/aguimera/PhyREC). The conversion of the recorded current signals (LPF and BPF) to a voltage signal was performed by summation of the two signals and inverse interpolation in the in vivo/chronic measured transfer curve of the corresponding gSGFET[17]. Even for large signals (tens of millivolts), this calibration method yields distortion-free signals, in contrast to using a fixed transconductance value[30]. Transfer curves were always measured at the beginning and end of every recording to ensure that no significant variations were present and to detect any malfunctioning transistor. Moreover, all recordings presented in the manuscript have been calibrated with the nearest-recorded transfer curve to ensure high fidelity in the voltage-converted signals.

To assess the detection limit in the conventional frequency bands (>1 Hz), baseline recordings were directly compared with post-mortem recordings (Fig. 2f). For instance, applying a digital filter (>200 Hz) and comparing post-mortem with baseline validates the ability of gDNP to record spontaneous high-frequency activity (>200 Hz) arising from groups of neurons in a non-pathological brain state (upper plot in Fig. 2f). Beyond this qualitative comparison, the SNR shown in Fig. 2f was evaluated from the ratio of the RMS mean value over 25 s of recording of baseline (spontaneous activity) and post-mortem (no activity) signals. The signals were BPF in three different bands, corresponding to local field potential activity (1–70 Hz), high-frequency activity (80–200 Hz) and very high-frequency activity (200–4,000 Hz). RMS values were calculated with a sliding window of 500 ms for the 1–70 Hz band and with a sliding window of 10 ms for the other two bands. The whisker plots were created with a Python library (seaborn.boxplot) to show the data distribution for working transistors in the gDNP (gDNP1 = 10, gDNP2 = 12, gDNP3 = 12 and gDNP4 = 14). In the whisker plots, the line in the box corresponds to the median value, the box shows the quartiles of the dataset and the whiskers extend to show the maximum and minimum values. The SNRs for the different bands were evaluated from a total of four in vivo experiments with four different gDNPs (Fig. 2f). The SNR is expressed in decibels ($20 \times \ln(\text{RMS}(S)/\text{RMS}(N))$), where S is the 'signal' during the baseline recording and N is the 'noise' measured during the post-mortem recording. The silencing of neuronal activity shown in Fig. 3d was extracted from the AC-coupled recording (HP-filtered, >0.5 Hz). Then, the RMS values of the pre-ictal phase (calculated with a sliding window of 1 s) were averaged over 50 s. A similar analysis was performed during the SD (15 s, shaded areas in Fig. 3d). The ratio of the two averaged RMS values corresponds to the neuronal activity variation (before and during the SD). The amplitudes of the hippocampal SD and the hyperpolarization wave in Fig. 3d were evaluated using the recording LPF in the infraslow regime (<0.5 Hz) and resampled at 3 Hz (instead of at 9.6 kHz, used in the original recording). The zero of the voltage was set using the mean value of the signal 50 s before the pre-ictal phase (Supplementary Fig. 9), and the minimum and maximum values for each channel were extracted (corresponding to the SD and hyperpolarization amplitude, respectively).

For the analysis of the DC-shifts pre-seizure (Fig. 3f and Supplementary Fig. 17), 20 min recordings starting from 1 min before the first seizure following 4-AP injection were selected. Seizures with concurrent high-amplitude depolarizations

such as SDs were excluded from analysis. The 20 min recordings were filtered in two bands: DC-coupled (LPF, <0.1 Hz) and seizure band (bandpass second-order filter, 4–12 Hz). Signals were downsampled to 96 Hz. The RMS value of the seizure band was calculated with a 0.5 s sliding window and used to determine seizure onset and end. Epochs around −5 to 2 s relative to seizure start of the DC-coupled signal were extracted for analysing the DC-shifts. Zero voltage was set to the mean of the first 2 s of the epoch, and the maximum amplitude of the period from −5 to 0 s was then extracted and used as the amplitude of the pre-seizure DC-shift.

CSD analysis applied to the low-frequency part of the potential (local field potential) was calculated with the Python open source Elephant library (Elephant Electrophysiology Analysis Toolkit) using the class 'Current Source Density analysis (CSD)', and the method 1D – StandardCSD was chosen for the linear gDNP array. A homogeneous conductivity of the neural tissue of $\sigma = 0.3$ S m⁻¹ across the different layers was used for the calculations.

The concurrency of ISO with the SWD shown in Fig. 4h was evaluated by performing the Hilbert transform to extract the phase of the DC-coupled signal (0.01–0.1 Hz) and associating it with the RMS in the range 5–9 Hz evaluated with a sliding window of 0.5 s (typical bandwidth for the SWD). Supplementary Fig. 16 shows in more detail the dependency of the ISO phase and SWD amplitude. The data shown in Fig. 4h illustrate the joint density probability, indicating the higher probability of a given RMS amplitude to ISO phase pair.

Chronic biocompatibility study. Details of the surgery, tissue collection, analysis of histology and data statistics used for the chronic biocompatibility study are provided in Supplementary Figs. 19 and 20.

Reporting Summary. Further information on research design is available in the Nature Research Reporting Summary linked to this article.

Data availability
All relevant data obtained to evaluate the main findings of the paper are openly available in Zenodo at https://doi.org/10.5281/zenodo.5655535. All other raw data are available from the corresponding author upon reasonable request.

Code availability
Python v.3.7 packages (Matplotlib v.3.2.0 and Numpy v.1.17.4) and the following Python library were used for electric characterization of the gSGFET arrays: https://github.com/aguimera/PyGFET. A custom Simulink model was used for graphene microtransistor electrophysiological data acquisition; contact g.tec medical engineering for code access. Electrophysiological data were analysed using Python v.3.7 packages (Matplotlib v.3.2.0, Numpy v.1.17.4, Pandas v.0.25.3, seaborn v.0.9.0, Neo v.0.8.0 and Elephant) and the custom library PhyREC (https://github.com/aguimera/PhyREC/tree/PhyREC4). Custom scripts can be found at Zenodo (https://doi.org/10.5281/zenodo.5655535). Immunohistochemical data analysis was performed using Python v.3.7 script (https://github.com/kebarr/biocompatibility_study).

References
50. Schaefer, N. et al. Improved metal-graphene contacts for low-noise, high-density microtransistor arrays for neural sensing. *Carbon* **161**, 647–655 (2020).
51. Jin, H. J. et al. Water-stable silk films with reduced β-sheet content. *Adv. Funct. Mater.* **15**, 1241–1247 (2005).
52. Rockwood, D. N. et al. Materials fabrication from Bombyx mori silk fibroin. *Nat. Protoc.* **6**, 1612–1631 (2011).
53. Vepari, C. & Kaplan, D. L. Silk as a biomaterial. *Prog. Polym. Sci.* **32**, 991–1007 (2007).
54. Cao, Y. & Wang, B. Biodegradation of silk biomaterials. *Int. J. Mol. Sci.* **10**, 1514–1524 (2009).
55. Gobin, A. S., Froude, V. E. & Mathur, A. B. Structural and mechanical characteristics of silk fibroin and chitosan blend scaffolds for tissue regeneration. *J. Biomed. Mater. Res. A* **74**, 465–473 (2005).
56. Russo, E. et al. Upholding WAG/Rij rats as a model of absence epileptogenesis: hidden mechanisms and a new theory on seizure development. *Neurosci. Biobehav. Rev.* **71**, 388–408 (2016).
57. van Luijtelaar, G. & van Oijen, G. Establishing drug effects on electrocorticographic activity in a genetic absence epilepsy model: advances and pitfalls. *Front. Pharmacol.* **11**, 395 (2020).

Author contributions

A.B.C. carried out most of the fabrication and characterization of the gDNPs, contributed to the design and performance of the in vivo experiments, analysed the data and wrote the manuscript. E.M.-C. contributed to the design and planning of the in vivo experiments, to the data analysis and particularly to the DC-shift and SD analysis of the in vivo data. R.C.W. and T.M.S. performed the in vivo experiments. D.R. contributed to the in vivo experiments and DC-coupled recordings with the glass micropipette. N.S., E.R.-L., X.I. and J.M.D.l.C. contributed to the fabrication and characterization of the gDNPs. E.D.C., J.B. and C.H. contributed to the growth, transfer and characterization of the CVD graphene used in the gDNPs. E.P.-A., A.H. and E.R.-L. contributed to the optimization of the SF stiffening protocol of the gDNPs. J.M.-A. contributed to the fabrication of the custom electronic instrumentation and development of a Python-based user interface. D.V. contributed to the Python scripts and technical discussions. J.R.S. reviewed the manuscript. J.F. and J.S. contributed to the mechanical assessment of the SF and the SF back-coated gDNPs. M.D. performed all surgeries for the biocompatibility study. A.D. and K.B. contributed to the capture of histological images and image processing and analysis. S.S. and K.B. contributed to the preparation and review of the manuscript. A.G.-B. contributed to the design and fabrication of the custom electronic instrumentation, the development of a custom gSGFET Python library and analysis of the data. R.V., K.K., R.C.W., A.G.-B. and J.A.G. participated in the design of all experiments and thoroughly reviewed the manuscript. All authors read and reviewed the manuscript.

Competing interests

C.G. is the owner of g.tec medical engineering and Guger Technologies. J.A.G, K.K and A.G.-B declare financial interest in INBRAIN Neuroelectronics. All other authors have no competing interests.

Additional information

Supplementary information The online version contains supplementary material available at https://doi.org/10.1038/s41565-021-01041-9.

Correspondence and requests for materials should be addressed to Rob C. Wykes, Anton Guimerà-Brunet or Jose A. Garrido.

Peer review information *Nature Nanotechnology* thanks Matthew Nelson, Bozhi Tian and the other, anonymous, reviewer(s) for their contribution to the peer review of this work.

Reprints and permissions information is available at www.nature.com/reprints.

nature portfolio

Corresponding author(s):   Rob Wykes, Anton Guimera and Jose A. Garrido

Last updated by author(s):   Oct 30, 2021

Reporting Summary

Nature Portfolio wishes to improve the reproducibility of the work that we publish. This form provides structure for consistency and transparency in reporting. For further information on Nature Portfolio policies, see our Editorial Policies and the Editorial Policy Checklist.

Statistics

For all statistical analyses, confirm that the following items are present in the figure legend, table legend, main text, or Methods section.

n/a	Confirmed	
☐	☒	The exact sample size (*n*) for each experimental group/condition, given as a discrete number and unit of measurement
☐	☒	A statement on whether measurements were taken from distinct samples or whether the same sample was measured repeatedly
☒	☐	The statistical test(s) used AND whether they are one- or two-sided *Only common tests should be described solely by name; describe more complex techniques in the Methods section.*
☒	☐	A description of all covariates tested
☒	☐	A description of any assumptions or corrections, such as tests of normality and adjustment for multiple comparisons
☐	☒	A full description of the statistical parameters including central tendency (e.g. means) or other basic estimates (e.g. regression coefficient) AND variation (e.g. standard deviation) or associated estimates of uncertainty (e.g. confidence intervals)
☒	☐	For null hypothesis testing, the test statistic (e.g. *F*, *t*, *r*) with confidence intervals, effect sizes, degrees of freedom and *P* value noted *Give P values as exact values whenever suitable.*
☒	☐	For Bayesian analysis, information on the choice of priors and Markov chain Monte Carlo settings
☒	☐	For hierarchical and complex designs, identification of the appropriate level for tests and full reporting of outcomes
☒	☐	Estimates of effect sizes (e.g. Cohen's *d*, Pearson's *r*), indicating how they were calculated

Our web collection on statistics for biologists contains articles on many of the points above.

Software and code

Policy information about availability of computer code

Data collection	Python 3.7 packages (Matplotlib 3.2.0, Numpy 1.17.4) and the following python library were used for electric characterization of the gSGFET arrays: https://github.com/aguimera/PyGFET. A custom simulink model was used for graphene microtransistor electrophysiological data acquisition, please contact g.tec medical engineering GmbH for code access.
Data analysis	All electrophysiological data were analysed using Python 3.7 packages (Matplotlib 3.2.0, Numpy 1.17.4, Pandas 0.25.3, seaborn 0.9.0, Neo 0.8.0, and Elephant 0.6.2) and the custom library PhyREC (https://github.com/aguimera/PhyREC/tree/PhyREC4). Custom scripts can be found at Zenodo link []. Immunohistochemical data analysis was performed using Python3.7 script (github.com/kebarr/biocompatibility_study).

For manuscripts utilizing custom algorithms or software that are central to the research but not yet described in published literature, software must be made available to editors and reviewers. We strongly encourage code deposition in a community repository (e.g. GitHub). See the Nature Portfolio guidelines for submitting code & software for further information.

Data

All relevant data obtained to evaluate the main findings of the paper are openly available in [repository name] at http://doi.org/[doi], reference number [xxxxx]. All other raw data are available from the corresponding author upon reasonable request.

Field-specific reporting

Please select the one below that is the best fit for your research. If you are not sure, read the appropriate sections before making your selection.

☒ Life sciences   ☐ Behavioural & social sciences   ☐ Ecological, evolutionary & environmental sciences

For a reference copy of the document with all sections, see nature.com/documents/nr-reporting-summary-flat.pdf

Life sciences study design

All studies must disclose on these points even when the disclosure is negative.

Sample size	Six wild-type adult male C57BL mice and four WAG-Rij rats were used in this study. No sample-size calculation was performed. Sample size was sufficient for proof-of-concept of gDNP technology. For the biocompatibility (histology and ELISA) studies where some prior knowledge about variability was available, we performed a power calculation indicating that groups of 3-4 animals at each time point would be required to sufficiently power these sets of experiments. For histological staining, all data sets are n=3, with the exception of 2-week graphene, which is n=4, and 12 weeks Neuronexus probes which are n=2, due to an inability to locate the probe location in histological sections for one animal implanted. For ELISA testing, gDNP with and without graphene hemisphere data sets are n=3 or 4 at all timepoints, while contralateral hemispheres were combined, giving n=7.
Data exclusions	Where statistical values are reported, no data was excluded. The exact sample size and whether data is obtained from the same or multiple subjects is mentioned in the text. Otherwise, data was selected for illustrative purposes of gDNPcapabilities.
Replication	All findings were replicated (see sample size), and the results reproducible. For histological staining, all data sets are n=3, with the exception of 2-week graphene, which is n=4, and 12 weeks Neuronexus probes which are n=2, due to an inability to locate the probe location in histological sections for one animal implanted. For ELISA testing, gDNP with and without graphene hemisphere data sets are n=3 or 4 at all timepoints, while contralateral hemispheres were combined, giving n=7. Electrophysiological signals recorded were very comparable across experimental units (animals), and transistors
Randomization	Randomization is not rellevant in our study since no conclusion is based on subject-dependent effects.
Blinding	All post-hoc biocompatibility analysis was performed by a researcher blind to the experimental condition. Electrophysiology data analysis did not require blinding as all animals were treated in the same way.

Reporting for specific materials, systems and methods

We require information from authors about some types of materials, experimental systems and methods used in many studies. Here, indicate whether each material, system or method listed is relevant to your study. If you are not sure if a list item applies to your research, read the appropriate section before selecting a response.

Materials & experimental systems

n/a	Involved in the study
☐	☒ Antibodies
☒	☐ Eukaryotic cell lines
☒	☐ Palaeontology and archaeology
☐	☒ Animals and other organisms
☒	☐ Human research participants
☒	☐ Clinical data
☒	☐ Dual use research of concern

Methods

n/a	Involved in the study
☒	☐ ChIP-seq
☒	☐ Flow cytometry
☒	☐ MRI-based neuroimaging

Antibodies

Antibodies used	1. Rabbit anti-Iba1 (1:1000, Wako 019-19741). 2. Chicken anti-GFAP (1:2000, Abcam ab4674). Secondary antibodies: 1.Anti-rabbit Alexa Fluor (AF) 560 2. Anti-chicken AF647 (all 1:500, Thermofisher).
Validation	Iba-1 (Wako 019-19741): IHC in rats is included https://labchem-wako.fujifilm.com/us/product_data/docs/00055446_doc02.pdf GFAP (Abcam ab4674): IHC in rats is included https://www.abcam.com/gfap-antibody-ab4674.html

Animals and other organisms

Policy information about studies involving animals; ARRIVE guidelines recommended for reporting animal research

Laboratory animals	C57BL/ mice were bred (2–4-month-old males), while WAG rats were imported (Charles river, used 6-9 month-old males). Animals were housed on 12 h/12 h dark/light cycle, and food and water were given ad libitum. Humidity was kept within 45% to 65% and temperature between 20⁰C to 24⁰C degrees. Prior to headbar surgery, animals were group housed, but after this, animals were individually housed. For the biocompatibility studies, adult male 6-8 weeks age Sprague-Dawley rats (230-280g) were used for this study (Charles River, England).
Wild animals	No wild animals were used in this study.
Field-collected samples	No field-collected samples were used in this study.
Ethics oversight	Electrophysiological recording experiments were conducted in accordance with the United Kingdom Animal (Scientific Procedures) Act 1986 and approved by the Animals in Scientific Research Unit at the Home Office (license PPL70-13691). Biocompatibility experimental procedures were conducted in compliance with the Animal welfare act, with approval of the Home Office and local animal welfare ethical review body (AWERB), license P089E2E0A.

Note that full information on the approval of the study protocol must also be provided in the manuscript.